Table S1. Overview of SLWC detection algorithms using MODIS and CloudSat. All profiles selected are ocean-only ('land_flag' = 2) with a solar zenith angle between 0 and 60°. MOD06-1KM-AUX R05 (Platnick et al., 2017) and 2B-GEOPROF R05 (Marchand et al., 2008) were used for MODIS and CloudSat products, respectively. ECMWF-AUX was used for cloud top temperatures (main text Sect. 2.3). Throughout the SLWC analysis, observational MODIS COT values were derived from the from the combination of unique profiles between 'Cloud_Optical_Thickness' and 'Cloud_Optical_Thickness_PCL' retrievals. Cloud top effective radius (R_e) was derived from the combination of unique profiles between the 'Cloud_Effective_Radius' and 'Cloud_Effective_Radius_PCL' retrievals.

Satellite Composite	A-Train Selection Criteria	E3SM-COSPv2.0 Selection Criteria	Diagnostic applications
MODIS and CloudSat	Based on the SLWC detection scheme described in Suzuki et al. (2010), with updated Cloud Optical Thickness (COT) threshold for consistency with COSPv2.0 WRDs: • CloudSat reflectivity profiles (2B-GEOPROF R05) are matched to MODIS cloud profiles (MOD06-1KM-AUX R05). • Cloud tops and bottom are determined where reflectivity > -30 dBZ. • Single layer clouds are selected where the MODIS cloud layer flag ('Cloud_Multi_Layer_Flag') indicates one layer and COT > 0.3. • MODIS cloud top pressure > 500 hPa. • MODIS cloud top effective radius $5 \leq R_e \leq 30$ µm • To select warm liquid clouds, the ECMWF-AUX temperature profiles were matched to the Cloud Profiling Radar (CPR) footprint. • Profiles are selected where the ECMWF-AUX cloud top temperature and MODIS cloud top temperature ≥ 273 K. • Profiles selected where CPR cloud mask ('cpr_cmask') values are ≥ 30, indicating a good or strong echo with high-	Based on the WRDs originally implemented in COSPv2.0 (Michibata et al., 2019), with modifications described in main text Sect. 2.2. Subcolumns selected where: • MODIS liquid water path (LWP) > 0 g/kg • MODIS liquid COT > 0.3 • MODIS Ice Water Path (IWP) ≤ 0 g/kg • MODIS ice COT < 0.3 • MODIS liquid cloud top effective radius $5 \leq R_e \leq 30$ µm • CloudSat reflectivity ≥ -30 dBZ for one or more contiguous layers • Temperature at cloud top (determined by CloudSat reflectivity threshold described above) ≥ 273 K	• SLWC cloud fraction maps, binned by CloudSat reflectivity • CFODDs binned by MODIS cloud top R_e • MODIS COT PDFs binned by MODIS cloud top R_e

Table S2. PI base cloud state for the 12 sensitivity experiments. Dash ("-") indicates the KK2000 coefficient value was unchanged from the default E3SMv2 parameterization (equal to the "CNTL" simulation value).

Name	A	α	β	accre	PI LWP (kg m^{-2})	PI SLWC Cloud Fraction	PI SWCRE (W m^{-2})
CNTL	3.05E+04	3.19	-1.4	1.75	0.107	0.052	-12.1
alpha01	-	4.22	-	-	0.180	0.049	-14.1
alpha02	-	3	-	-	0.080	0.052	-10.7
beta01	-	-	-1		0.087	0.050	-10.4
beta02	-	-	-1.79	-	0.124	0.052	-13.0
beta03	-	-	-3.01	-	0.161	0.051	-14.1
acoef0.05x	1.35E+03	-	-	-	0.150	0.052	-13.9
acoef5x	1.53E+05	-	-	-	0.079	0.050	-10.1
acoef10x	3.05E+05	-	-	-	0.066	0.047	-8.9
acoef50x	1.53E+06	-	-	-	0.039	0.034	-5.2
acoef100x	3.05E+06	-	-	-	0.030	0.026	-3.6
accre	-	-	-	5	0.077	0.049	-10.2

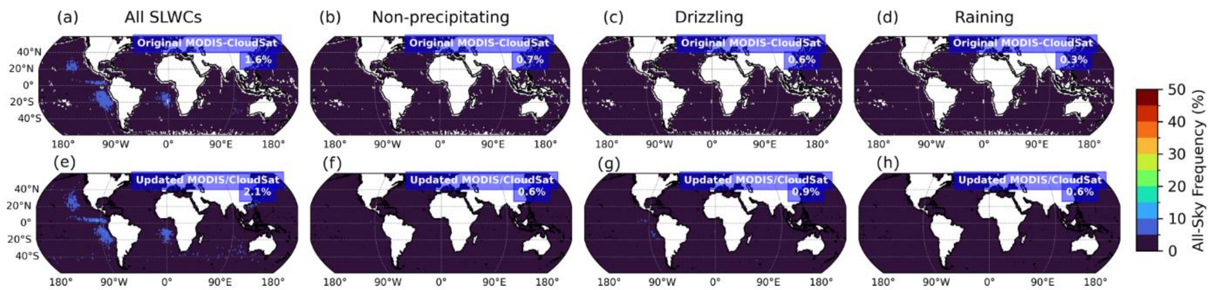

Figure S1. All-sky frequencies of total SLWCs June 2006 – Apr 2011, non-precipitating ($Z_{max} < -15\ dBZ_e$), drizzling ($-15\ dBZ_e \leq Z_{max} < 0\ dBZ_e$) and raining ($Z_{max} \geq 0\ dBZ_e$) ocean-only SLWCs according to original reference analysis of MODIS and CloudSat observations (Michibata et al., 2019a, 2019b) (a-d), and updated reference MODIS and CloudSat analysis (as in Fig. 1), but increasing the lower MODIS COT threshold from 0.3 to 15.

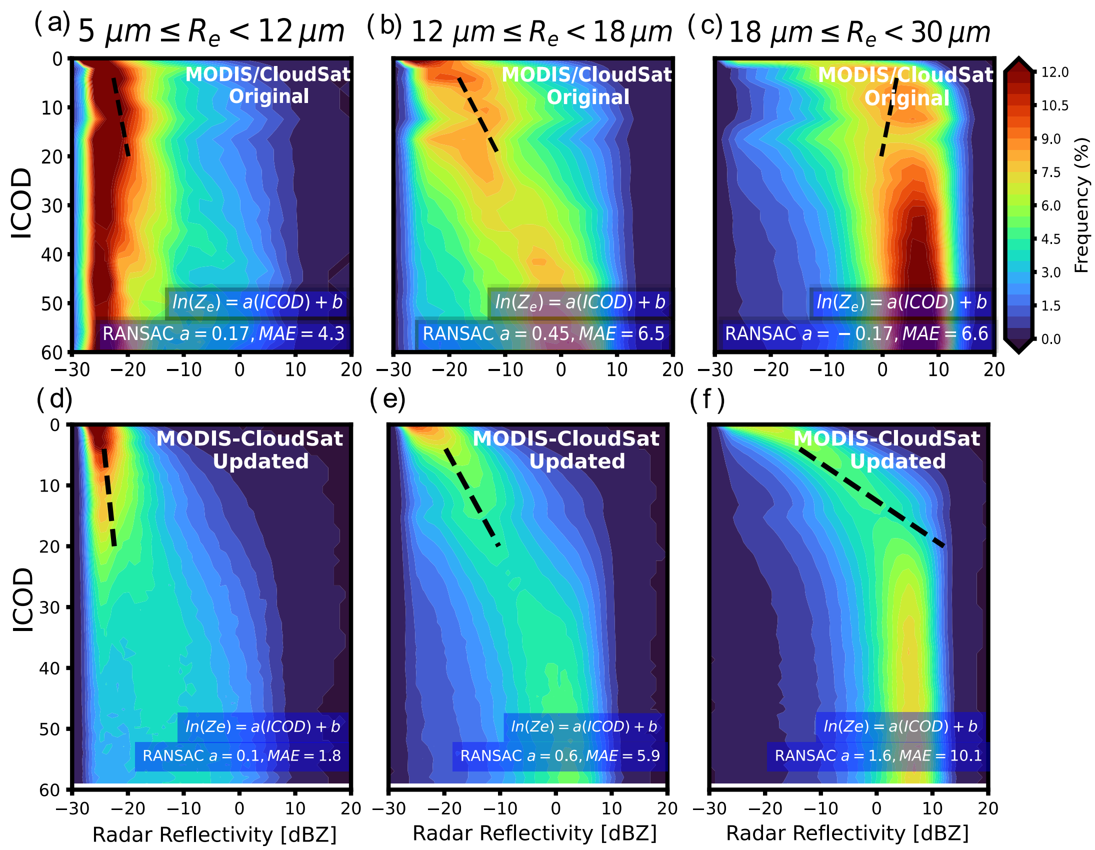

Figure S2. Contoured frequency by optical depth diagrams (CFODDs) for SLWCs June 2006 – April 2011 binned by MODIS cloud top effective radius (R_e) from original reference MODIS-CloudSat observations analysis (a-c) and updated reference MODIS-CloudSat observations analysis (d-f) as in Fig. 2, but increasing the lower MODIS COT threshold from 0.3 to 15. Random Sample Consensus (RANSAC) linear regressions were applied to the CFODD at 4 ≤ ICOD ≤ 20 to estimate droplet collection efficiencies. RANSAC slopes and Median Absolute Error (MAE) values are shown in blue boxes.

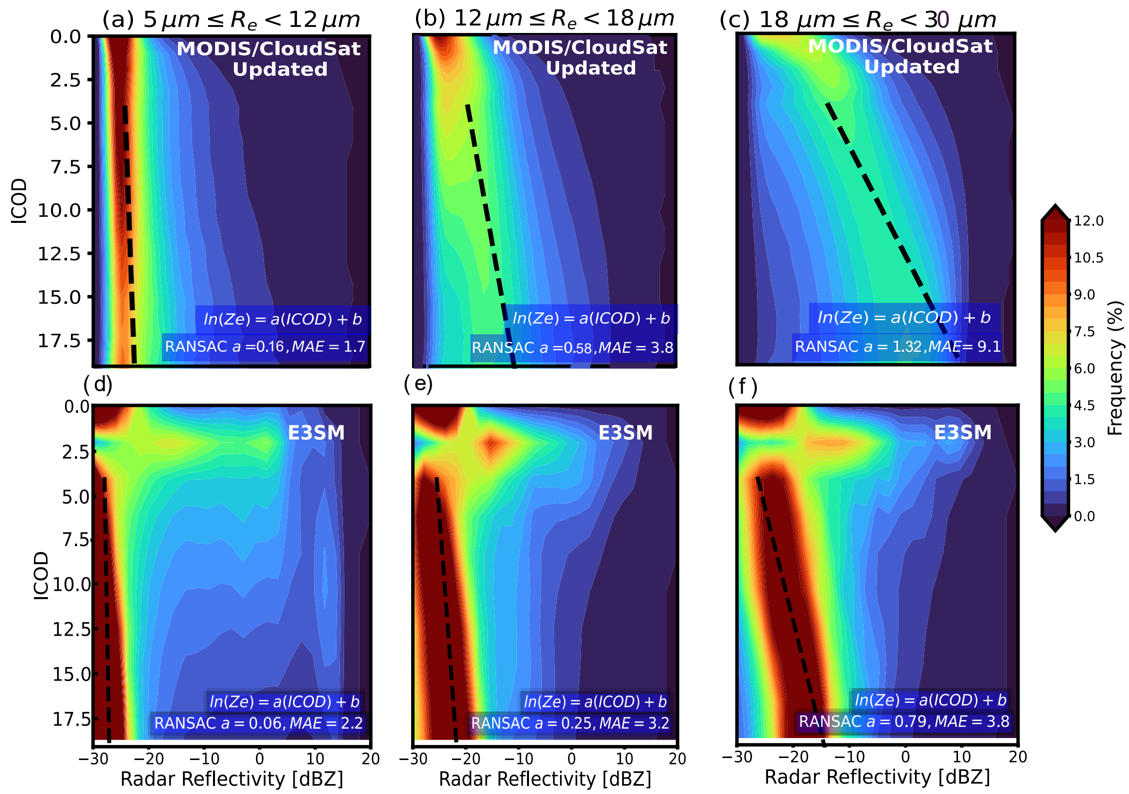

Figure S3. Contour frequency by optical depth diagrams (CFODDs) for subset of SLWCs with max CloudSat reflectivity < 20 dBZ and COT < 20, June 2006 – April 2011 binned by MODIS cloud top effective radius (R_e) from updated reference MODIS-CloudSat observations analysis (a-c) and the E3SMv2 simulation (d-f). CloudSat reflectivities are binned by MODIS in-cloud optical depth (ICOD) to construct CFODDs. Random Sample Consensus (RANSAC) linear regressions were applied to the CFODD at $4 \leq$ ICOD ≤ 20 to estimate droplet collection efficiencies. RANSAC slopes and Median Absolute Error (MAE) values are shown in blue boxes. E3SM-COSP CFODDs shows discontinuity in CloudSat reflectivity frequencies near cloud top, and decreased droplet collection efficiencies compared to observations.

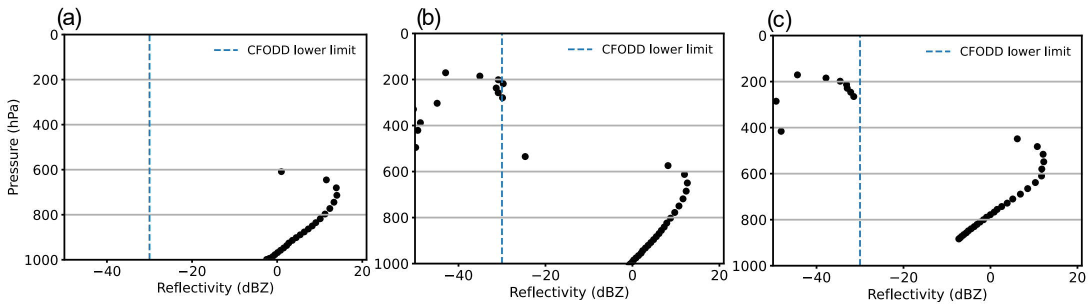

Figure S4. Example E3SMv2 SLWC reflectivity profiles from the CloudSat simulator output in COSPv2.0. E3SMv2 SLWCs exhibit reflectivity > 0 dBZ at cloud top with high frequency compared to MODIS-CloudSat observations (see Fig. 2, Sect. 3). A CloudSat ground-clutter mask that was implemented in the WRDs for improved comparison with observations is not shown here.

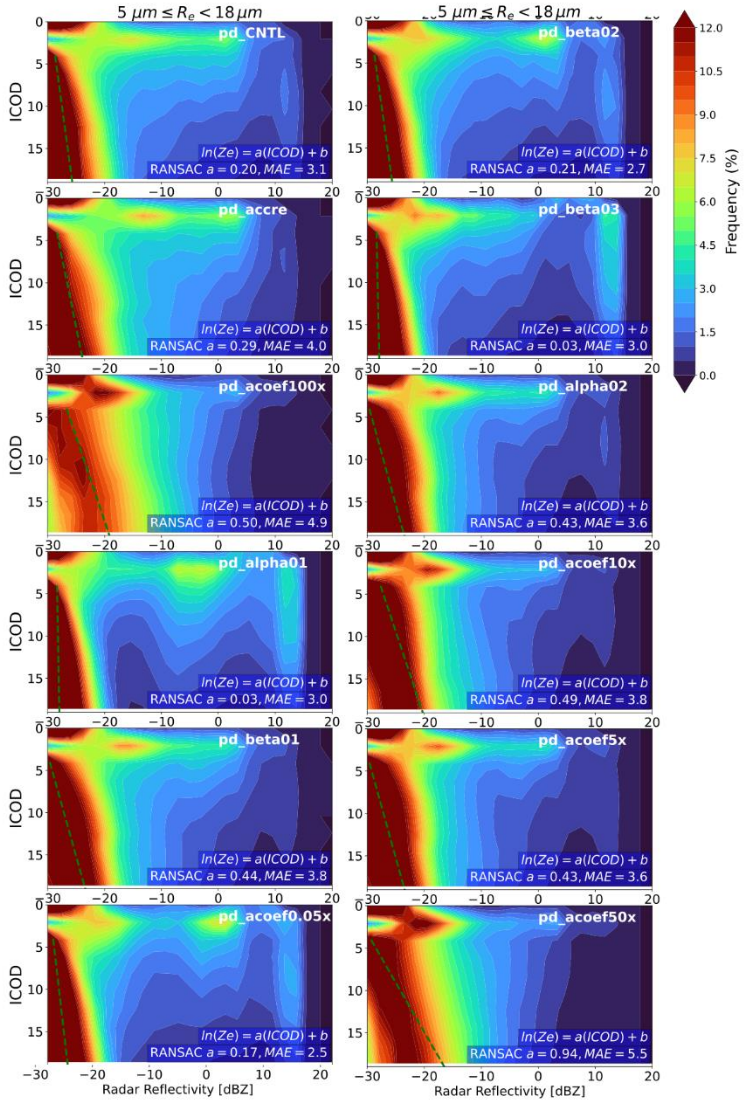

Figure S5. CFODDs for E3SMv2 PD simulations in 12 experiments featuring variations of the default E3SMv2 autoconversion and accretion parameterizations (Table 1), for SLWCs with MODIS R_e between 5 and 18 μm and COT between 4 and 20. RANSAC linear regressions were applied to the CFODDs at $4 \leq ICOD \leq 20$. RANSAC slopes and MAE values are shown in blue boxes.

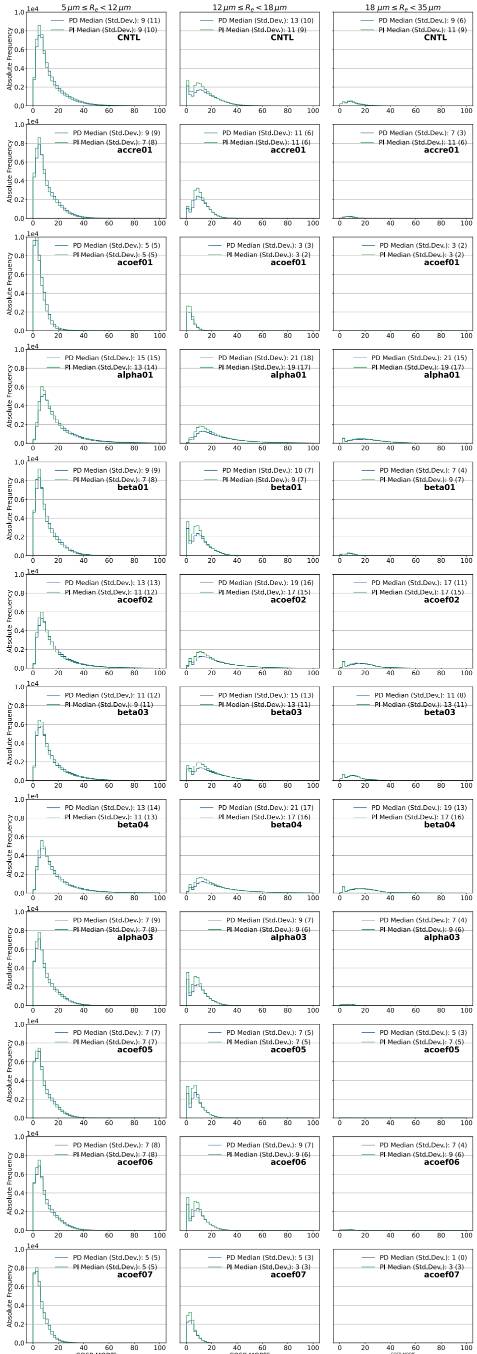

Figure S6. Absolute frequency of SLWCs in E3SMv2 in 12 warm rain process sensitivity experiments, binned by simulated MODIS R_e. Blue and green PDFs indicate the PD and PI simulation results, respectively.

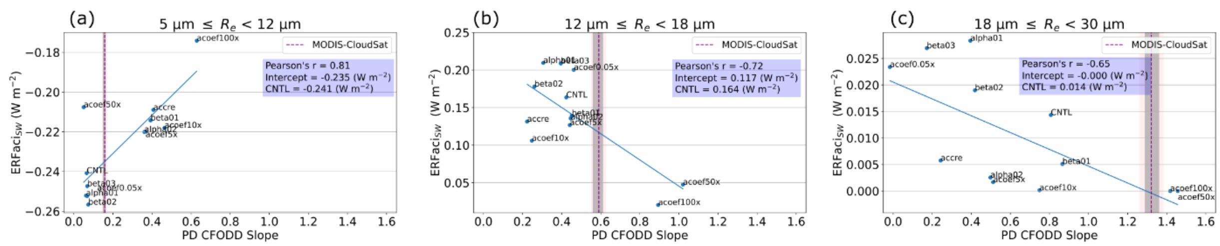

Figure S7. Linear regression between E3SMv2 ERFaci$_{SW}$ and CFODD slopes in 12 PD autoconversion and accretion sensitivity experiments, binned by MODIS R_e. Results show that SLWCs in the small and medium R_e size bin contribute to ERFaci$_{SW}$ in equal magnitude but opposite sign, and SLWCs with large R_e make a relatively small positive contribution to ERFaci$_{SW}$ compared to the small or medium R_e populations. The positive correlation in the small R_e size bin indicates that increasing droplet collection efficiency weakens ERFaci$_{SW}$ for this SLWC subset. The positive ERFaci$_{SW}$ values that diminish with increasing CFODD slope in the medium and large R_e size bins indicate that increased aerosol yields decreased small and medium Re SLWC cloud fraction (see Figs. S12-S13), but that increased droplet collection efficiencies oppose the aerosol effect. Grey and pink shaded regions indicate the 68 and 98% confidence intervals for the MODIS-CloudSat CFODD slope, respectively. Labels indicate the sensitivity experiment names (Table 1).

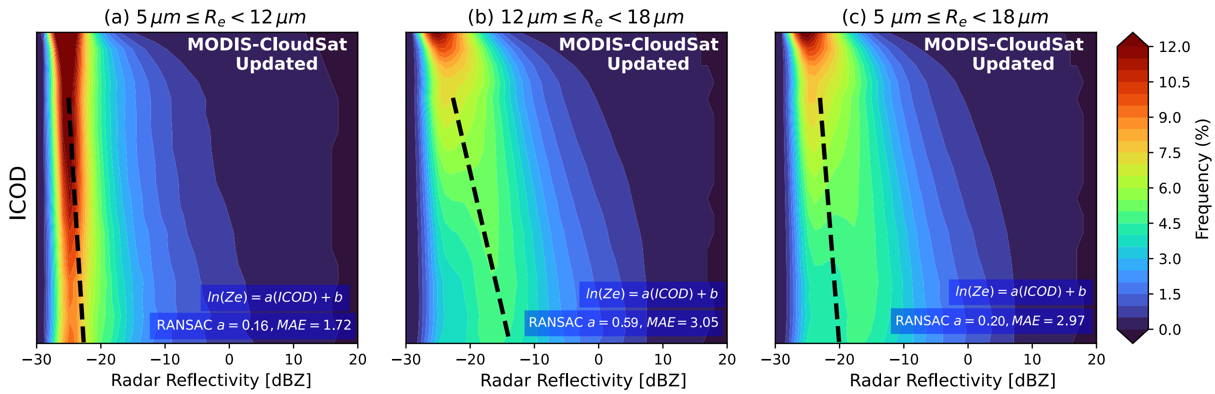

Figure S8. CFODDs as in Fig. S3 for subset of SLWCs with max CloudSat reflectivity < 20 dBZ and COT < 20, June 2006 – April 2011 binned by MODIS R_e from updated reference MODIS-CloudSat observations analysis (a-c), but with combined "small" and "medium" Re SLWCs in (c). CloudSat reflectivities are binned by MODIS ICOD to construct CFODDs. Random Sample Consensus (RANSAC) linear regressions were applied to the CFODD at $4 \leq$ ICOD ≤ 20 to estimate droplet collection efficiencies. RANSAC slopes and Median Absolute Error (MAE) values are shown in blue boxes.

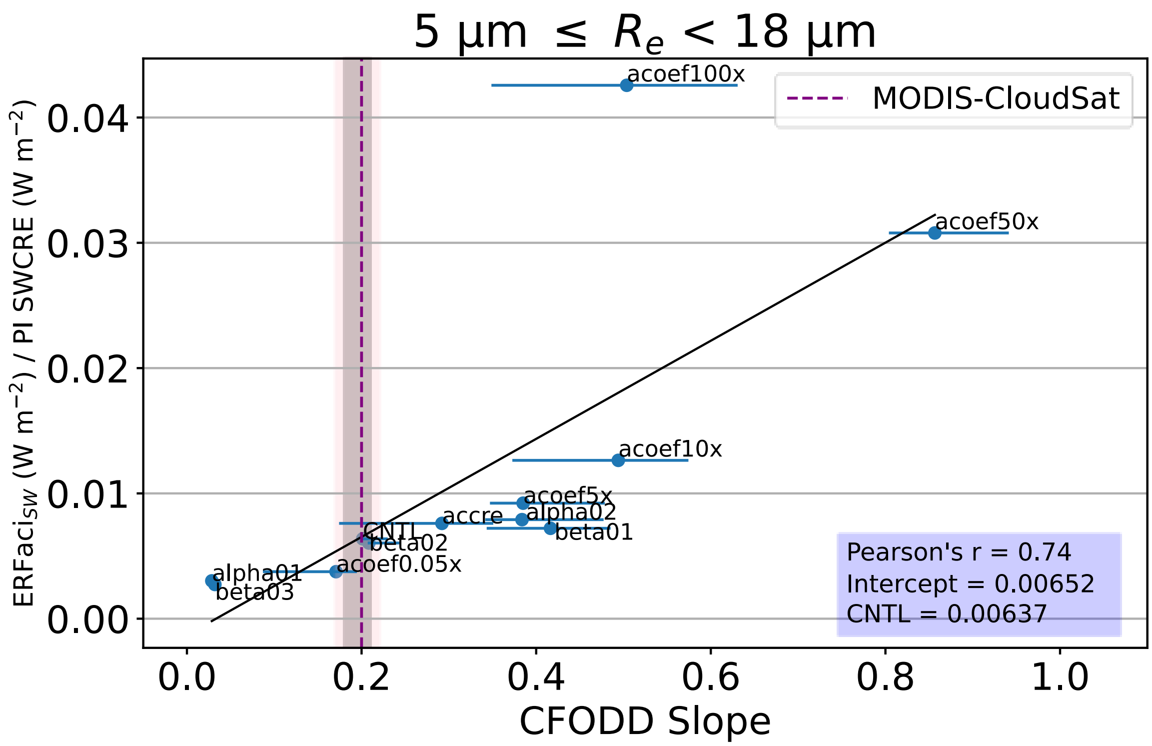

Figure S9. Linear regression between E3SMv2 ERFaci$_{SW}$ normalized by SWCRE and CFODD slopes in 12 PD autoconversion and accretion sensitivity experiments, generated from SLWCs with MODIS R_e between 5 and 18 µm. Error bars represent 1-sigma error estimated from RANSAC-fit bootstrapping (Sect. 2). Grey and pink shaded regions indicate the 68 and 98% confidence intervals for the MODIS-CloudSat CFODD slope, respectively. Labels indicate the sensitivity experiment names (Table 1).

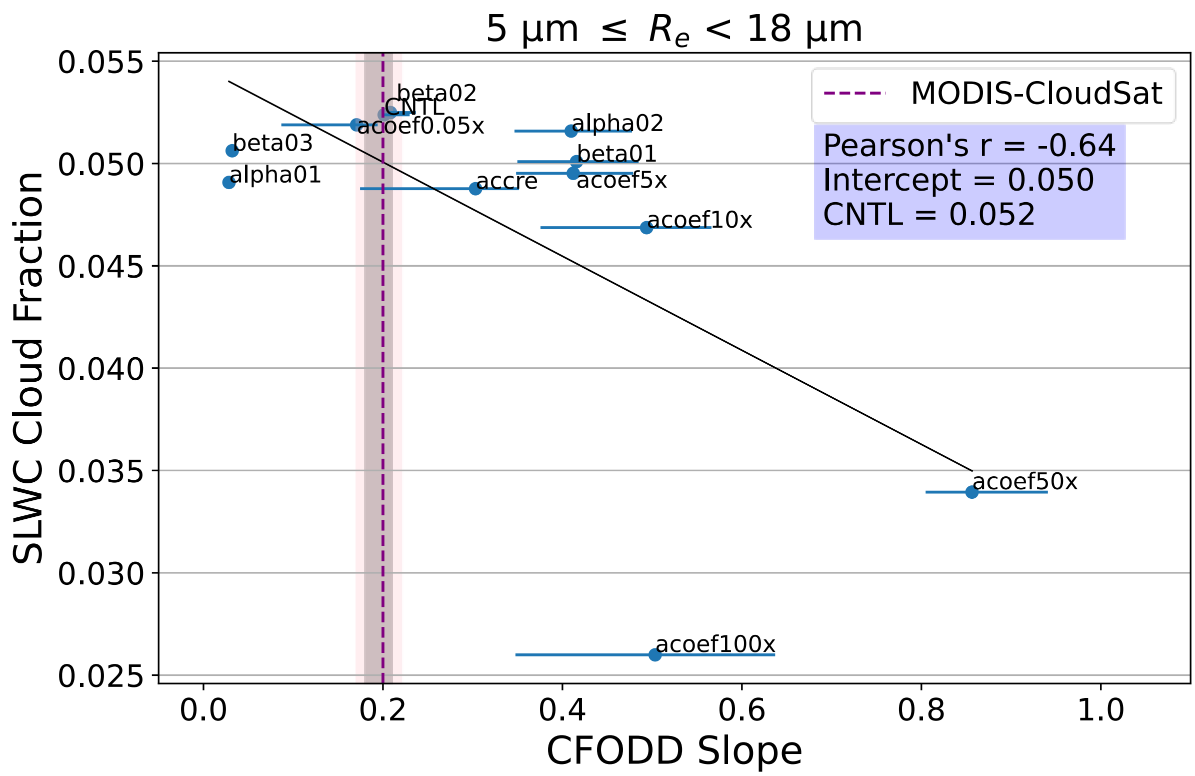

Figure S10. Linear regression between PI E3SMv2 SLWC cloud fraction and PD CFODD slopes in 12 autoconversion and accretion sensitivity experiments, generated from SLWCs with MODIS R_e between 5 and 18 µm. Error bars represent 1-sigma error estimated from RANSAC-fit bootstrapping (Sect. 2). Grey and pink shaded regions indicate the 68 and 98% confidence intervals for the MODIS-CloudSat CFODD slope, respectively. Labels indicate the sensitivity experiment names (Table 1).

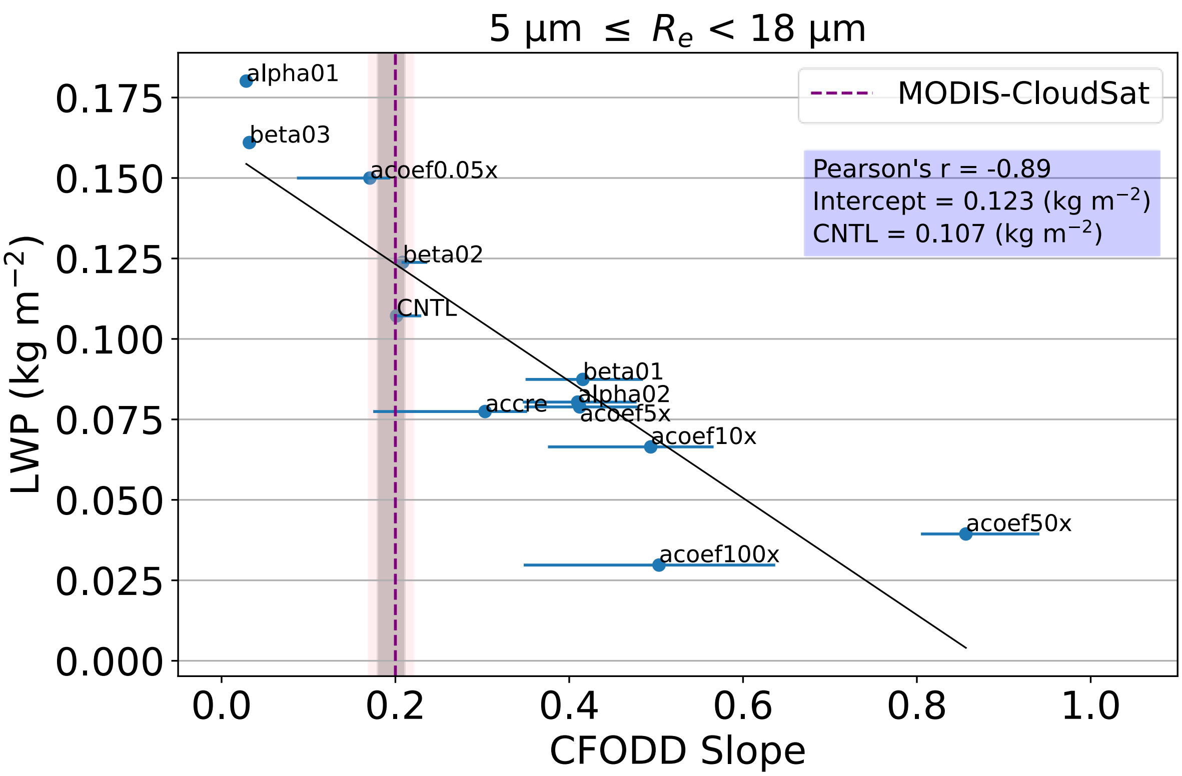

Figure S11. Linear regression between PI E3SMv2 SLWC LWP and PD CFODD slopes in 12 autoconversion and accretion sensitivity experiments, generated from SLWCs with MODIS R_e between 5 and 18 µm. Error bars represent 1-sigma error estimated from RANSAC-fit bootstrapping (Sect. 2). Grey and pink shaded regions indicate the 68 and 98% confidence intervals for the MODIS-CloudSat CFODD slope, respectively. Labels indicate the sensitivity experiment names (Table 1).

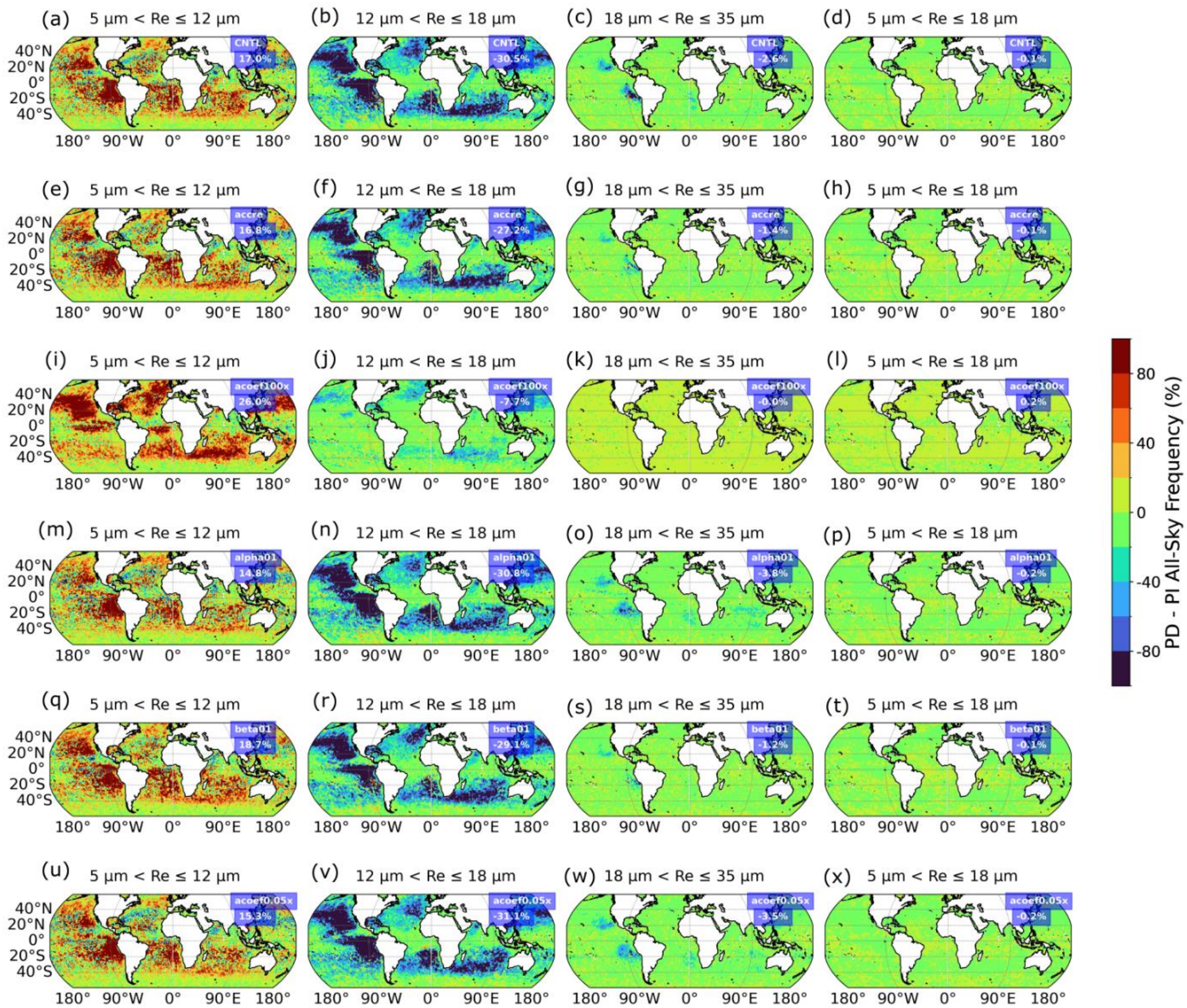

Figure S12. Difference between PD and PI all-sky SLWC cloud fraction in 6 of 12 warm rain process sensitivity experiments, binned by simulated MODIS R_e. Labels indicate experiment name (Table 1) and global mean cloud fraction difference.

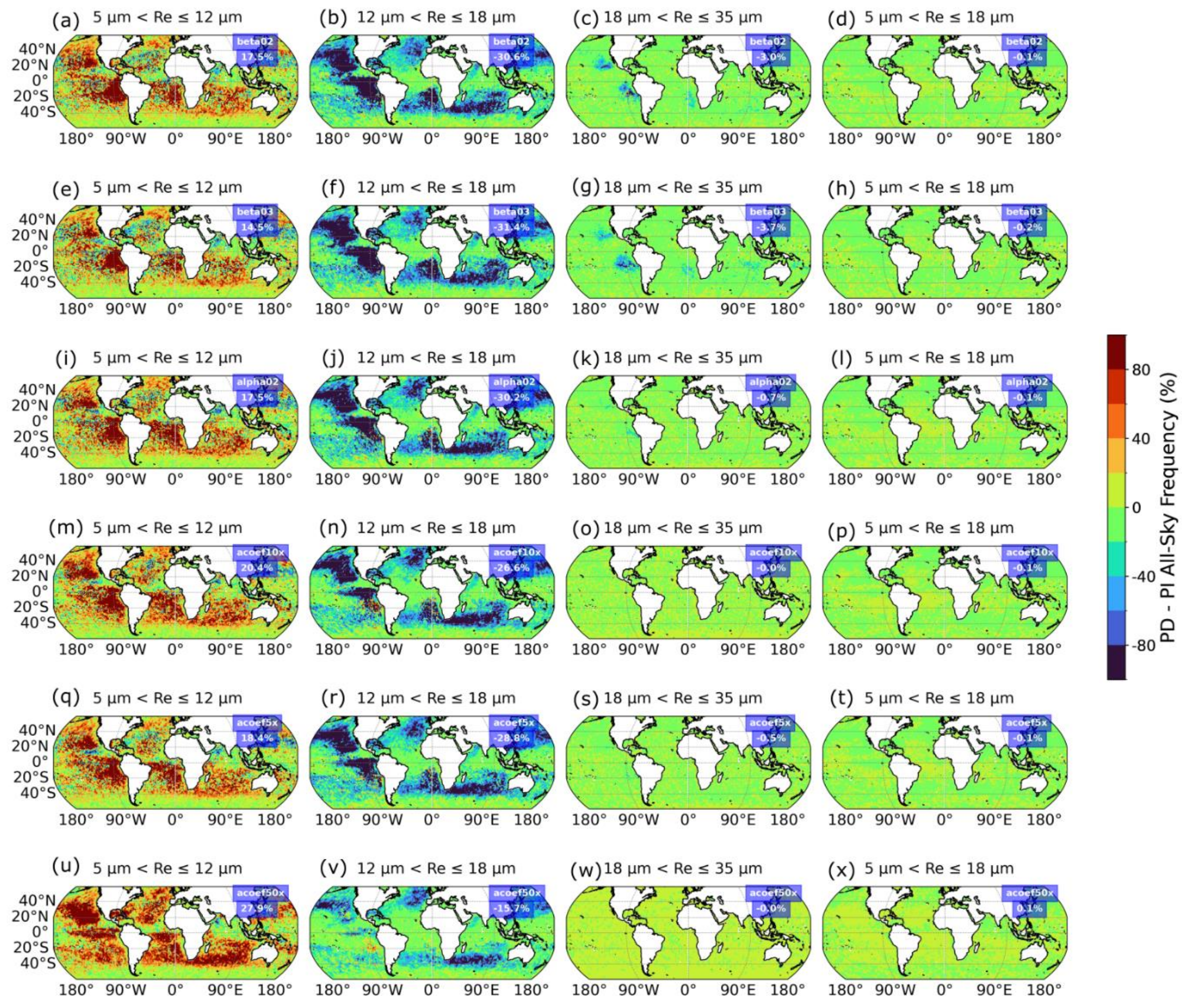

Figure S13. Difference between PD and PI all-sky SLWC cloud fraction in 6 of 12 warm rain process sensitivity experiments, binned by simulated MODIS R_e. Labels indicate experiment name (Table 1) and global mean cloud fraction difference.

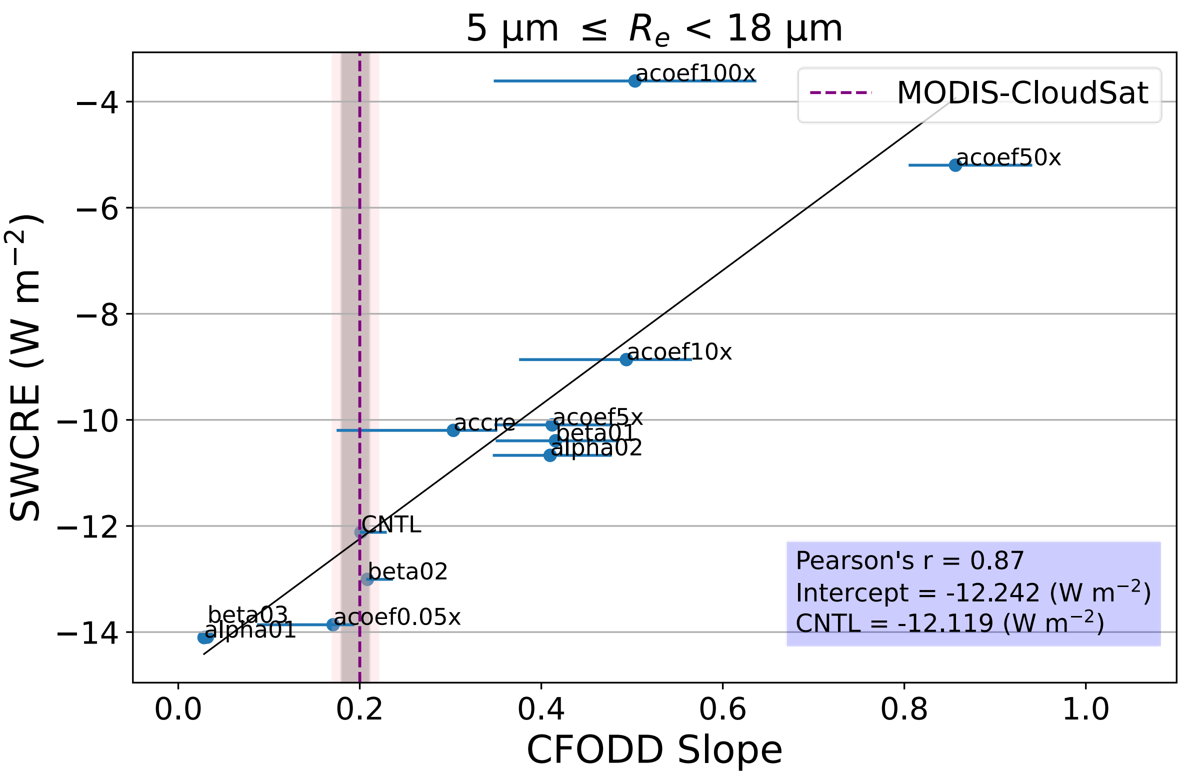

Figure S14. Linear regression between PI E3SMv2 SLWC SWCRE and PD CFODD slopes in 12 autoconversion and accretion sensitivity experiments, generated from SLWCs with MODIS R_e between 5 and 18 µm. Error bars represent 1-sigma error estimated from RANSAC-fit bootstrapping (Sect. 2). Grey and pink shaded regions indicate the 68 and 98% confidence intervals for the MODIS-CloudSat CFODD slope, respectively. Labels indicate the sensitivity experiment names (Table 1).

References

Mace, G. G., & Zhang, Q. (2014). The CloudSat radar-lidar geometrical profile product (RL-GeoProf): Updates, improvements, and selected results. *Journal of Geophysical Research: Atmospheres*, *119*(15), 9441–9462. https://doi.org/https://doi.org/10.1002/2013JD021374

Marchand, R., Mace, G. G., Ackerman, T., & Stephens, G. (2008). Hydrometeor Detection Using Cloudsat—An Earth-Orbiting 94-GHz Cloud Radar. *Journal of Atmospheric and Oceanic Technology*, *25*(4), 519–533. https://doi.org/10.1175/2007JTECHA1006.1

Michibata, T., Suzuki, K., Ogura, T., & Jing, X. (2019a). Incorporation of inline warm rain diagnostics into the COSP2 satellite simulator for process-oriented model evaluation. *Geoscientific Model Development*, *12*(10), 4297–4307. https://doi.org/10.5194/gmd-12-4297-2019

Michibata, T., Suzuki, K., Ogura, T., & Jing, X. (2019b). Incorporation of inline warm rain diagnostics into the COSP2 satellite simulator for process-oriented model evaluation. *Geoscientific Model Development*, *12*(10), 4297–4307. https://doi.org/10.5194/gmd-12-4297-2019

Platnick, S., Meyer, K. G., King, M. D., Wind, G., Amarasinghe, N., Marchant, B., Arnold, G. T., Zhang, Z., Hubanks, P. A., Holz, R. E., Yang, P., Ridgway, W. L., & Riedi, J. (2017). The MODIS Cloud Optical and Microphysical Products: Collection 6 Updates and Examples From Terra and Aqua. *IEEE Transactions on Geoscience and Remote Sensing*, *55*(1), 502–525. https://doi.org/10.1109/TGRS.2016.2610522

Suzuki, K., Nakajima, T. Y., & Stephens, G. L. (2010). Particle Growth and Drop Collection Efficiency of Warm Clouds as Inferred from Joint CloudSat and MODIS Observations. *Journal of the Atmospheric Sciences*, *67*(9), 3019–3032. https://doi.org/10.1175/2010JAS3463.1